Boundary layer chemical vapor synthesis of self-organized radial filled-carbon-nanotube structures

F. S. Boi[1], G. Mountjoy[2], and M. Baxendale[1*]

[1]School of Physics and Astronomy, Queen Mary University of London, Mile End Road, London,

E1 4NS, UK

[2]School of Physical Sciences, University of Kent, Canterbury, CT2 7NH, UK

*Correspondence to: m.baxendale@qmul.ac.uk

Abstract

We report a new chemical vapor synthesis method that exploits random fluctuations in the viscous boundary layer between a laminar vapor flow and a surface to yield a not previously observed product: radial ferromagnetically filled-carbon-nanotube structures departing from a central particle. The filling of the nanotube capillary is continuous over a scale much greater than that which can be achieved by conventional CVD. This is a simple method which does not require ultra-fine control of process parameters or highly-engineered reactor components in which a single, self-organized, ordered product is formed in randomly fluctuating vapor in the boundary layer by vapor-, liquid-, solid-phase self-organization. These fluctuations create the thermodynamic conditions for formation of the central particle in the vapor which in turn defines the spherically symmetric diffusion gradient that initiates the radial growth. The subsequent radial growth is driven by the supply of vapor feedstock by local diffusion gradients created by endothermic graphitic carbon formation at the vapor-facing tips of the individual nanotubes and

is halted by contact with surface. The radial structures are the dominant product and the reaction conditions are self-sustaining. We argue that the method has potential for scalable production of metal-carbon nanostructures with other unusual morphologies.

1. Introduction

The production of graphite-encapsulated transition metal nanocrystals has a long history of investigation owing to the range of applications for single domain, nanoscale magnetic particles that are chemically and mechanically protected from the environment. Production has been dominated by a variation of the Krätschmer-Huffman evaporation process, which played a central role in the production of fullerenes and nanotubes [1], in which metal-carbon species are evaporated from transition-metal-containing graphitic electrodes and the desired products – spherical or faceted graphite-encapsulated nanocrystals – are collected on the chamber walls. The collected products, in the form of a 3D web, soot or agglomerations, contain minority nanoscale carbonaceous products with spring-like, tubular, fiber, graphitic platelet, or irregular, radial structures comprising unfilled carbon nanotubes departing from a central metal particle – often referred to as 'urchins'– as well as unencapsulated metal nanoparticles [2]. The diversity of products results from the dynamic inhomogeneities in the arc plume of evaporated species that result in multiple spatial pathways with differing metal-carbon concentrations, thermal histories, and length- and time-scales within the arc chamber. The local thermodynamics within a single pathway activates a dominant formation mechanism from many simultaneously competing mechanisms to yield the nanoscale product at the collection point. The severe temperature gradient between the electrodes and reactor walls within the arc chamber drives vapor flow to the collection point; this has the advantage of damping of dynamic fluctuations by the resultant

diffusion gradients. Thermal fluctuations can be damped by the selection of the inert background gas on the basis of heat capacity. However, the arc method inevitably produces multiple nanoscale products owing to the inherent dispersion of spatial pathways.

Elliott et al. took the cumulative evidence from arc-produced material to formulate a model linking possible formation mechanisms to processing parameters for any vapour-phase process that forms nanoparticles in the presence of gaseous carbon [2]. It identified the local-pathway carbon-to-metal ratio – it selects which formation mechanisms are active along each pathway within the reactor – and the global carbon-to-metal ratio of species – which places bounds upon and determines the weighting between different pathways – as the factors that determine the distribution of products within the collected, macroscopic product. A low carbon-to-metal ratio is synonymous with a high nanoparticle count due to spontaneous formation of particles of a critical radius in saturated vapour when the free energy released by bulk formation is sufficient to sustain the surface [3]. This study produced a unified product map detailing the range of nanoscale structures as a function of nanoparticle count (Fig.3 in Ref. 2).

The formation mechanism descriptions are based on the same vapor-, liquid-, and solid-phase chemistry and catalysis at transition metal surface models that underpin mass production methods for unfilled carbon nanotubes by catalytic CVD [2, 4-7]. These mechanisms are not fully understood and remain controversial but the most widely-accepted general features can be stated as follows: i) there is exothermic catalytic decomposition of hydrocarbons at the surface of the transition metal nanoparticles at elevated temperature (the nanoparticle is assumed to be fully formed, liquid-state metal- or metal-carbon nanoparticle), ii) the carbon species dissolve

into the metal nanoparticle until the solubility limit at that temperature is reached whereupon iii) the carbon precipitates on the surface and exothermically crystallizes into energetically stable graphitic carbon, iv) alternatively, a high carbon flux at the nanoparticle surface can also result in graphitic shell formation, and iv) the temperature gradient created by the exo- and endo-thermal processes beneficially drives the flow of dissolved carbon in the particle as described below.

In view of these features, the formation mechanism-selecting role of the local carbon-to-metal ratios of a pathway within a reactor becomes clear, as do the features of the unified product map. A low value will result in a high metal nanoparticle count and consequently rapid consumption of carbon feedstock from the vapour driven by the inward, radial diffusion gradient created by the dissolution of carbon species in individual nanoparticles. The temperature gradient created by the exothermic shell-formation process drives the flow of carbon within the particle to the surface where it graphitizes. The most likely product is, therefore, a metal nanocrystal encapsulated in a graphitic shell. The diameter of the encapsulated nanoparticle is fixed by the critical radius for spontaneous particle formation, the subsequent growth due to exposure to vapor and the diameter at saturation [2]. The growth of the particle is, therefore, 'switched off' by elimination of the temperature gradient within the particle by either cessation of graphitic shell formation by consumption of all internal carbon, or thermal equilibrization with the vapour or contact with an cold surface.

A higher carbon-to-metal ratio, on the other hand, favours lower-energy nanotube nucleation and growth from fewer nanoparticles; here the temperature gradient is created by the exothermal catalytic decomposition at the vapor-facing nanoparticle surface and the exothermic graphitic

carbon formation at the circumference, carbon feedstock is driven through the nanoparticle to the forming nanotube by the subsequent diffusion gradient. The nanotube diameter is fixed by the lowest energy configuration for the cylindrical graphitic tube for a given nanoparticle diameter and the length is determined by the duration of exposure to a constant vapour supply (the so called residence time) or by contact with a cold surface.

The highest carbon-to-metal regime of the unified product map is the realm of the urchin, spring-like, and platelet products. The irregularity of the urchin structures observed in the arc-produced material suggests nanotube nucleation on the surface of a nanoparticle of larger diameter than those of the radiating nanotubes and nanotube growth in a non-spherical diffusion gradient for carbon species. The difficulty of achieving the latter by arc production is the reason why urchins are a minority product by this method. The arc-produced spring-like, and platelet nanoscale products are most likely to be the result of growth from a solid-phase, faceted nanoparticle as achieved by CVD using preformed nanoparticles so are most likely to be the products of the pathways with the thermal profile for the solidification of liquid nanoparticles [8].

CVD and aerosol methods have the advantage of local pathway control by streamlining reactor design and careful selection and control of process parameters; these methods have, therefore, largely replaced arc-production as the dominant approach to guaranteeing single reaction products [6,7].

The quest for radial carbon nanostructures has been driven by potential application as nanofillers for polymer-based nanocomposite materials since the large surface area is predicted to

dramatically enhance mechanical properties [9]. Previously observed carbon nanotube urchins comprise irregular, unfilled nanotubes centered on metal nanoparticles in the minority products of arc-discharge or PECVD reactors [10,11] or were intentionally formed by exposure of preformed particles of zeolite, nanodiamond, or other particles to hydrocarbon vapor at elevated temperature in a CVD process [12-16]. Metal nanoparticle-centered unfilled radial carbon nanotube growth has been achieved by an aerosol method which uses multiple precursor gasses, laminar flows, and a multiple temperature-zone reactor to sequentially achieve central-particle formation and radial growth [17]. Although two reports remark on partial filling of small numbers of individual nanotubes in urchin structures, there have been no previous reports of macroscopic quantities of radial filled-carbon-nanotube structures [10,11].

Multiwall carbon nanotubes filled with nanocrystals of the elemental phases, alloys, or carbides of transition metals are conventionally produced in steady-state conditions by flowing the products of metallocene ($M(C_5H_5)_2$, where M is a transition metal) decomposition over smooth, inert surfaces at elevated temperature in the isothermal reaction zone of a horizontal CVD reactor [18-40]. The decomposed metallocene vapor contains transition metal, hydrocarbon, and hydrogen species ($Fe(C_5H_5)_2 \rightarrow Fe+ H_2 + CH_4 + C_5H_6+\ldots$, [18]) that react on the surface to form the nucleating metal particles from which the nanotube and nanocrystalline filling simultaneously grow perpendicular to the substrate in closely packed vertical arrays. As with all conventional CVD methods, the local vapor pathway is defined by the spatial extent of the steady-state concentration gradient that is established perpendicular to the surface as the growing array consumes species from the vapor (chemical equilibrium); the lateral vapor velocity at the surface is zero [3]. The local carbon-to-metal ratio is, therefore, determined by the relative rates

of diffusion of the species in this concentration gradient. The global vapor pathway is defined as that with finite lateral vapor velocity many diffusion lengths away from the growing array. In steady-state vapor flow, the global carbon-to-metal ratio is ultimately defined by that of the individual metallocene molecule hence the method produces a single nanoscale product. The lateral velocity in the global flow determines the rate of supply of species to the diffusion gradient and hence the rate of growth of the array which in turn fixes the spatial extent of the diffusion gradient. In this way the global flow places bounds on the local pathway in accordance with the conclusions that underpin the unified product map outlined above.

This conventional CVD approach profoundly differs from the arc and aerosol methodologies in that the nucleation is on a liquid metal particle made non-spherical by wetting of the surface (heterogeneous nucleation) consequently the energetics of formation are very different from particle formation in vapor (homogeneous nucleation) [3]. The role of the surface is, therefore, to provide a constant wetting angle through smoothness on the scale of the nanoscale product and inert, invariant surface chemistry over the desired area. A consequence of the array being in contact with a surface (the reactor wall) is that the array will grow in the natural thermal gradient between the wall and the center of the reactor whereas in arc and aerosol reactors thermophoresis causes migration within this gradient. The aspects of the formation mechanism for which there is a general agreement are sequentially: i) decomposition of the hydrocarbons by the nucleating metal particle is followed by dissolution of carbon in the nanoparticle and nucleation of a nanotube at saturation, ii) metal and carbon species in the vapor feed the vertical growth of both the nanotube and the filling from the base or the open tip (or both) of the nanotube, and iii) the multiple nanotube walls are created by outward diffusion of carbon from the central capillary.

Since the structures grow in the natural temperature gradient of the reactor, the role of the exo- and endo-thermic processes is not clear.

The magnetic response of these hybrid structures is dominated by that of the ferromagnetic filling since the graphitic carbon of the nanotube walls is weakly diamagnetic [41]. There are numerous potential applications owing to the ability to tune the magnetic response through the composition and shape anisotropy of the filling [42-44]: magnetic storage media [45], drug delivery systems, nanoscale containers for biomedical diagnosis, therapy, and monitoring [46], nanoscale inductors [47], probes for magnetic force microscopy [48], nanocomposite magnetic filler particles [49], buckypaper [50], and microwave absorption materials [51, 52]. Other applications exploit the torque on the structures when placed in a constant magnetic field [53], or the oscillatory motion when placed in a time-varying magnetic field [54].

The main barrier to realising these applications is the poor nanocrystal length and continuity control achievable with existing synthesis methods, particularly when the nanotube length is greater than several micrometres. Steady-state CVD conditions are employed to guarantee nanowire continuity but result in discontinuous filling with isolated nanocrystals of length less than one-micrometre [18-40]. We speculate that specifically local pathway carbon-to-metal ratio fluctuation, that is perturbation of the vertical diffusion gradient by uneven growth in the array, is the cause of nanocrystal discontinuity since other fluctuations (global pathway, global carbon-metal ratio, thermal), as argued above, are relatively stable.

Here we report a new chemical vapor synthesis method that seeks to exploit rather than eliminate local pathway fluctuations to yield a not previously observed structures, ferromagetically filled-carbon-nanotube urchins, as the dominant reaction product where both the central particle formation and radial filled-carbon-nanotube growth occur spontaneously in randomly fluctuating vapor in the viscous boundary layer between a rough surface and the laminar vapor flow in a conventional horizontal CVD reactor. The vapor flow on the scale of the roughness is dominated by viscous forces which result in non-zero lateral vapor velocity at the tips of salient features and randomly fluctuating eddies [55]. Surface roughening can also profoundly influence the heat transfer to the vapor and contribute to thermal fluctuation within a local pathway [56].

This is a simple, scalable method which does not require ultra-fine control of process parameters or any highly-engineered reactor components. The role of the rough surface is to intentionally induce a local region of randomly fluctuating vapor close to the laminar flow to create the conditions for both the nucleation of a central particle and subsequent growth.

We later propose a growth mechanism and argue that the method has great potential for production of carbon nanostructures with other morphologies.

2. Experimental

2.1 Synthesis

A steady-state global vapor pathway was created by flowing the products of the thermal decomposition of ferrocene ($Fe(C_5H_5)_2$) in a horizontal CVD reactor. The source vapor was produced by sublimation of 60 mg of ferrocene powder using a coil preheater and carried in a laminar argon flow within a quartz tube (length: 2 m, outer diameter: 22 mm, inner diameter: 18 mm, wall thickness: 2 mm) at atmospheric pressure inside a one-zone electrical furnace with an isothermal reaction zone at 990 °C. The maximum temperature of the preheater was 180 °C. The duration of the reaction was 4.5 minutes. The reactor was cooled to room temperature at the natural rate of the furnace. The reaction product was the expected close-packed vertical arrays of iron-filled multiwall-carbon-nanotubes on smooth quartz surfaces.

However, under identical conditions, the introduction of a rough quartz surfaces yielded thick deposits comprising ensembles of individual urchins, Figs.1, 2. The surfaces were prepared by roughening a quartz substrate using a conventional diamond cutting tool to produce multi-scale roughness with a peak-to-valley distance of ~100 μm. Optimum results were achieved with an argon flow rate of 3 - 20 ccm. The average Reynolds number for the ferrocene vapor flow was estimated to be Re=2-4; well within the range for laminar flow, Re<2000 [56]. The deposition area was ~1 cm^2 and the outcome was reproduced many tens of times. Vertical-to-radial growth regions were observed at smooth- rough quartz substrate boundaries, inset Fig.2.
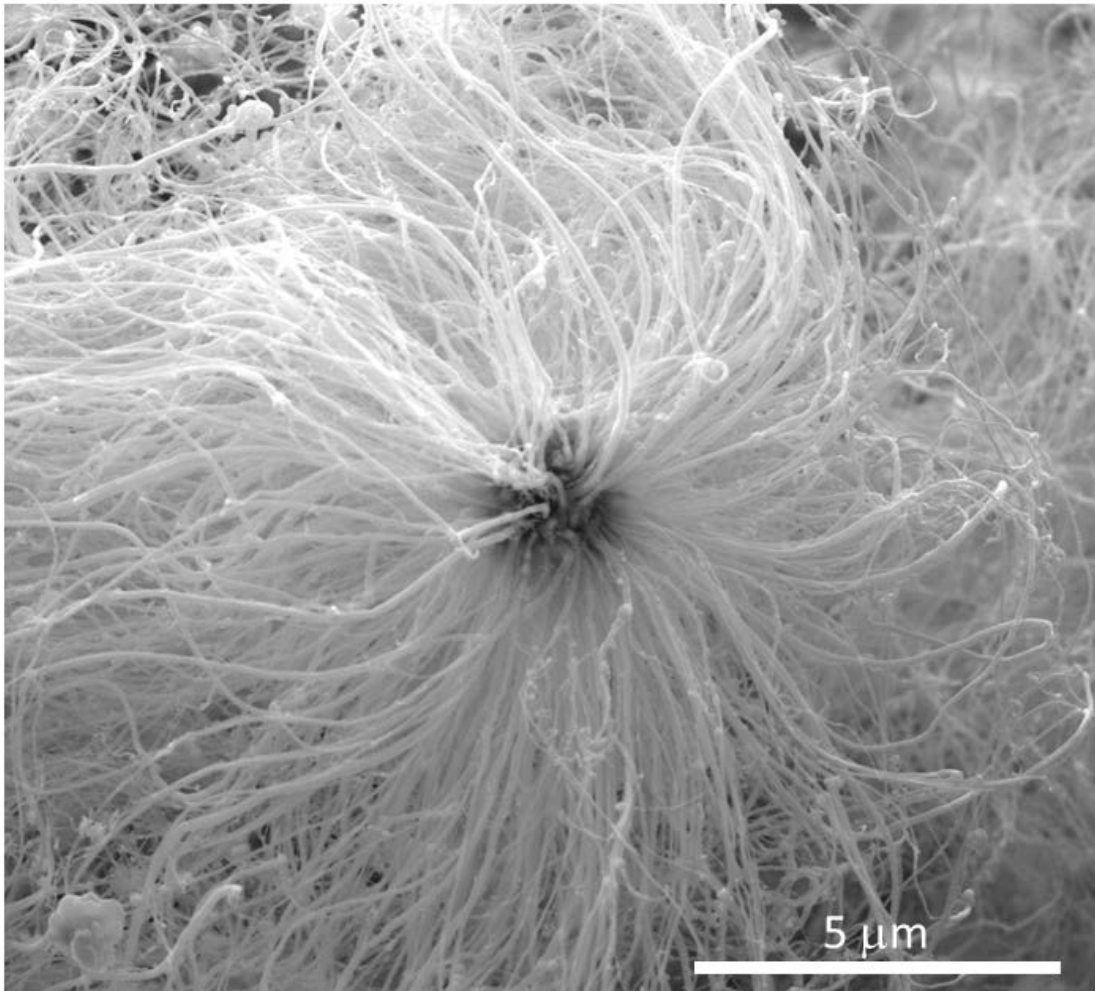
Fig.1: A scanning electron micrograph of an urchin comprising radial filled multiwall-carbon-nanotubes departing from a central particle.
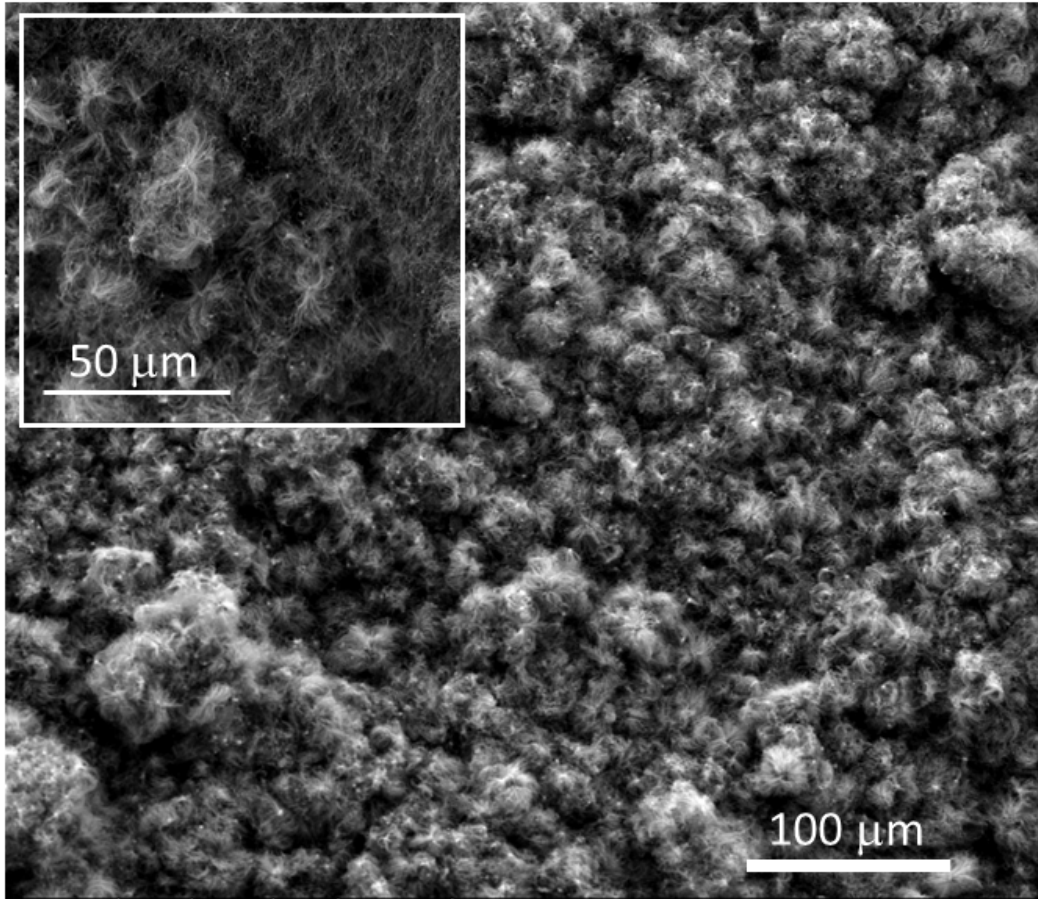
Fig.2: A scanning electron micrograph of the thick deposit of urchins on the rough quartz surface. The inset shows a distinct vertical-to-radial growth region at smooth-rough quartz substrate boundary: the upper-right region is the top view of a vertical array of filled multiwall-carbon-nanotube grown perpendicular to the smooth quartz surface, and the lower-left is that of layers of free-standing urchins on rough quartz surface.

2.2 Structural characterization

X-Ray diffraction analyses were performed with a Siemens D5000 diffractometer and with an Xpert-Pro diffractometer (both with Cu K_α source). The Rietveld refinement method, which uses the least-squares approach to match a theoretical line profile to the diffractogram, was used to identify and estimate the relative abundances of the phases from the area enclosed by the diffraction peaks. Scanning electron microscopy investigations were performed using an FEI Inspect F system. Transmission electron microscopy (TEM) and selective area electron diffraction (SAED) were performed using a 200 kV Jeol Jem 2010. The TEM samples were prepared by transferring the urchins to carbon-coated copper grids. The lattice spacings extracted from the SAED analyses have an accuracy of ±0.01 nm. The magnetic measurements of the powder containing the urchins were performed at 5 K with a MPMS-7 squid magnetometer (Quantum Design).

3. Results and discussion

The average diameter of the urchins was ~13 μm. The thickness of the deposit was many times the diameter of an individual urchin. The deposit was easily mechanically or magnetically removed and readily dispersed in alcohol. The ease of removal of the deposits suggests weak adhesion to the rough quartz surface, weak inter-structural forces, and no covalent cross-linking. Consideration of the spherical symmetry of the both the central particles and the complete individual urchins, and the above observations, strongly point to the following conclusions: i) the complete structure was spontaneously nucleated and formed in the boundary layer region, ii) the urchin growth is 'switched off' by contact with the surface or underlying urchin deposit, and iii) the vapor fluctuation created by an urchin deposit on the roughened surface is comparable to that of the original rough surface; the reaction conditions are self-sustaining and, therefore, scalable.

Electron microscopy revealed the complex structure of the urchin, Fig.3-5. Analysis of fifty central particles revealed the majority had diameter 1.5±0.3 μm; the minimum and maximum observed diameters were 0.4 and 3 μm, respectively. The central particle – the point of departure for the radial filled nanotubes – is an agglomeration of approximately spherical nanoparticles of 100-150 nm diameter comprising graphite-encapsulated Fe_3C nanocrystals with an inter-graphitic-shell spacing of 0.33 nm, Figs. 4(B), 5. According to the unified product map, such structures are produced by the widest range of process parameters; and have previously been produced by both steady-state and explosive syntheses [57, 58].
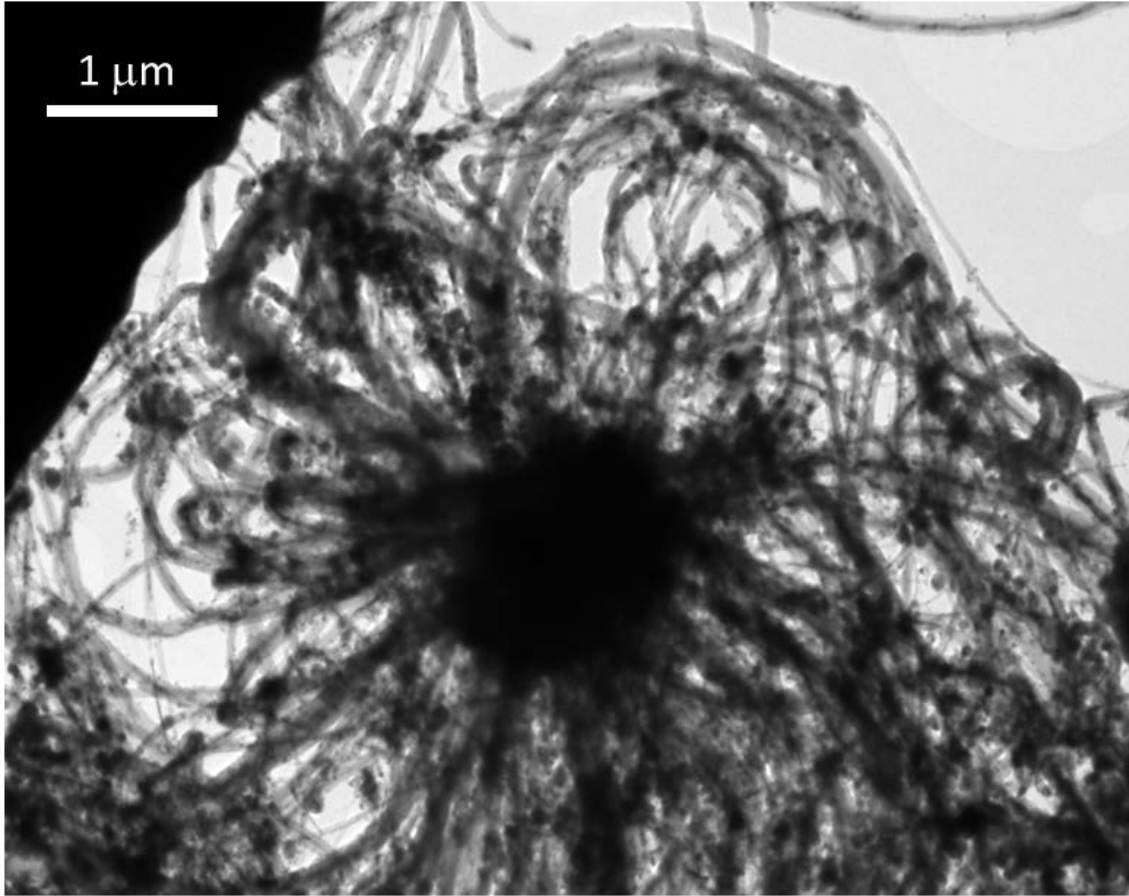
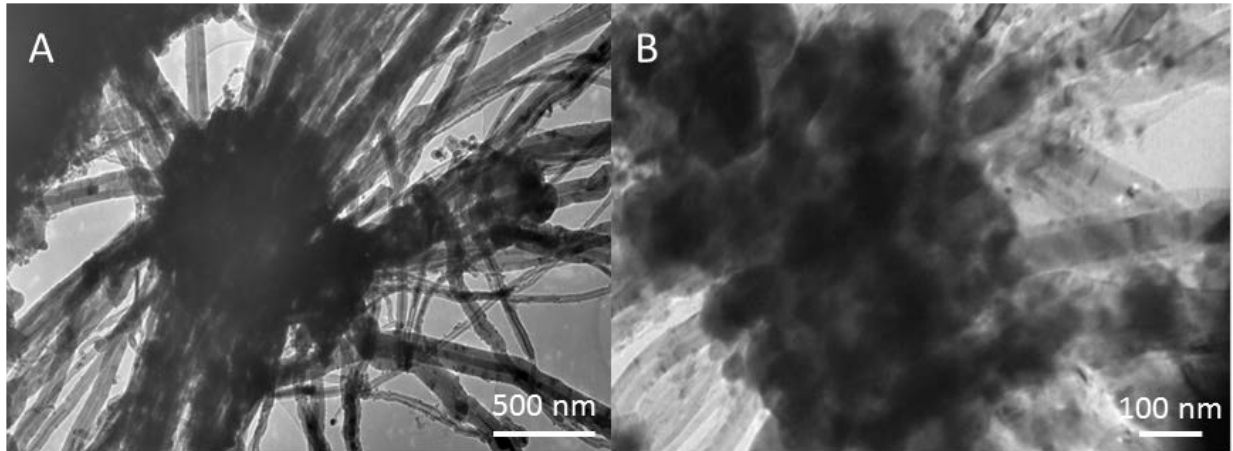Fig. 3: Transmission electron micrograph of an urchin. The central particle has a diameter of ~1μm.

Fig.4: A transmission electron micrographs of: (A) a typical urchin showing the ~ 1μm diameter central particle and the departing filled multiwall-carbon-nanotubes. The encapsulated crystalline nanocrystal contrasts with the nanotube walls; and (B) a small central particle composed of an agglomeration of approximately spherical coated nanoparticles.
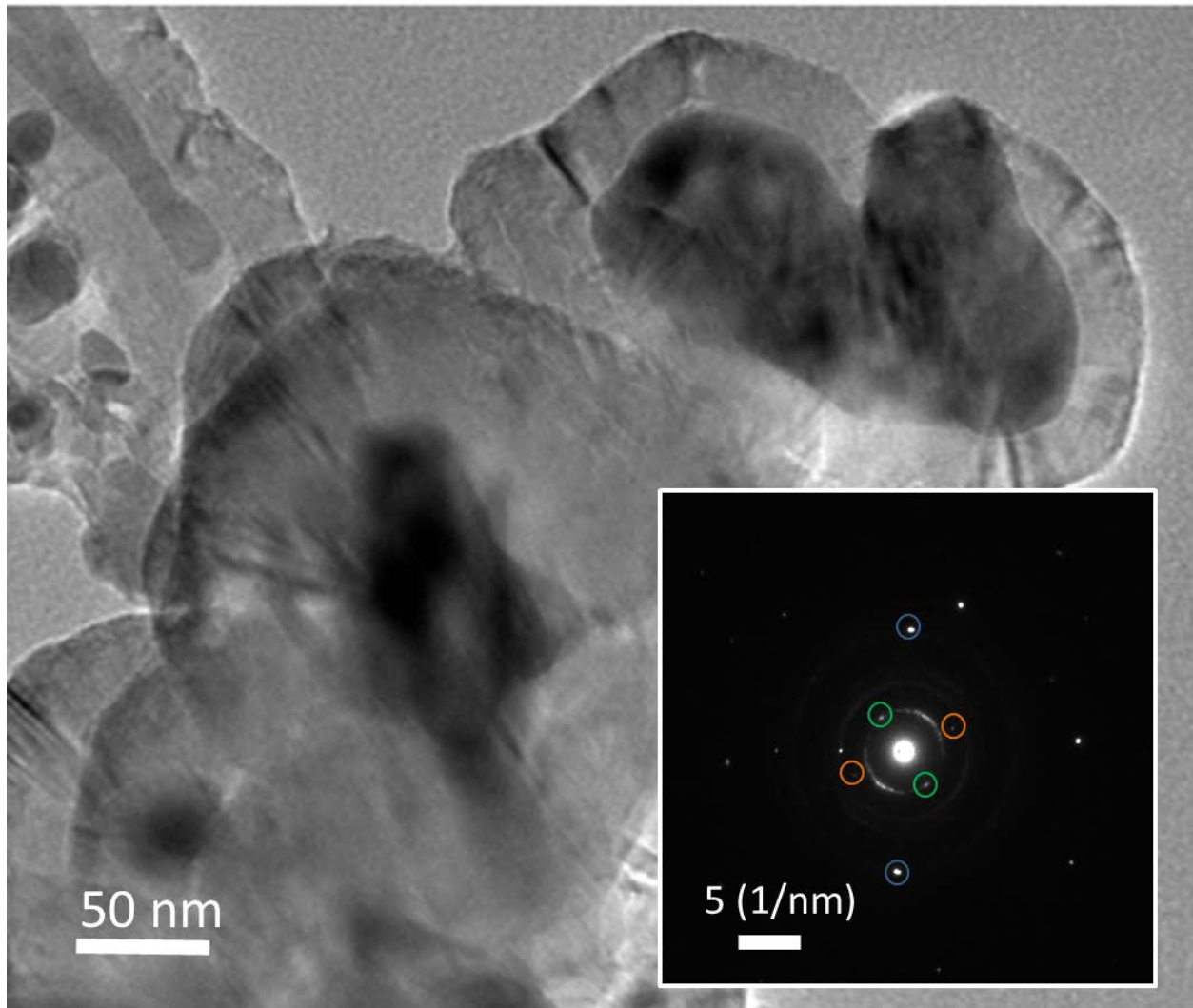
Fig.5: Transmission electron micrograph of small particles (~100 nm) observed in the central particle of a small urchin. Inset: selective area diffraction pattern obtained from one of the spherical particles. The orange circles indicate a lattice spacing of 0.25 nm corresponding to the (200) plane of Fe_3C with space group Pnma. The blue circles indicate a lattice spacing of 0.11 nm corresponding to the (303) plane of Fe_3C with space group Pnma. The green circles indicate the spots corresponding to the (002) lattice planes of graphite with spacing 0.33 nm.

The radial multiwall-carbon-nanotubes encapsulate nanocrystals with a high degree of continuous filling, Fig. 6. The synthesis routes for vertical structures reported in the literature generally use steady-state conditions to guarantee nanowire continuity but result in less than 1 μm nanowire lengths [18-40]. In contrast the encapsulated nanowires in the radial structures are continuous for at least 9 μm, Fig.6.

The nanotube inter-wall spacing was that typical for graphitic nanostructures, 0.34 nm, Figs. 7-9. The difference between the directly observed inter-graphitic-layer spacing of the spherical graphite-encapsulated Fe_3C nanocrystals and the nanotube walls (0.33 nm and 0.34 nm, respectively) was manifest as two proximate peaks in X-ray diffractograms, Fig. 10.

The main encapsulated phases were identified as those commonly observed in the vertical arrays, namely α-Fe, and γ-Fe, and Fe_3C, Figs. 8, 9 [18-40]. Unlike the vertical array structures, the radial structures have a very low abundance of Fe_3C; the iron carbide content diminishes with increasing vapour flow rates used in the reaction. With a vapor flow rate of 20 ccm there was essentially no γ-Fe present, Fig. 9.

The demarcation between the central particle formation and the onset of growth of the radial filled nanotubes (that is, the urchin) is likely to be the result of the asymmetry in exposure to the vapor [59]. That is, the rapid formation of the central particle means that the partially formed spherical particles on the exterior of the central particle are exposed to vapor feedstock flow driven by the diffusion gradient directed toward the central particle.
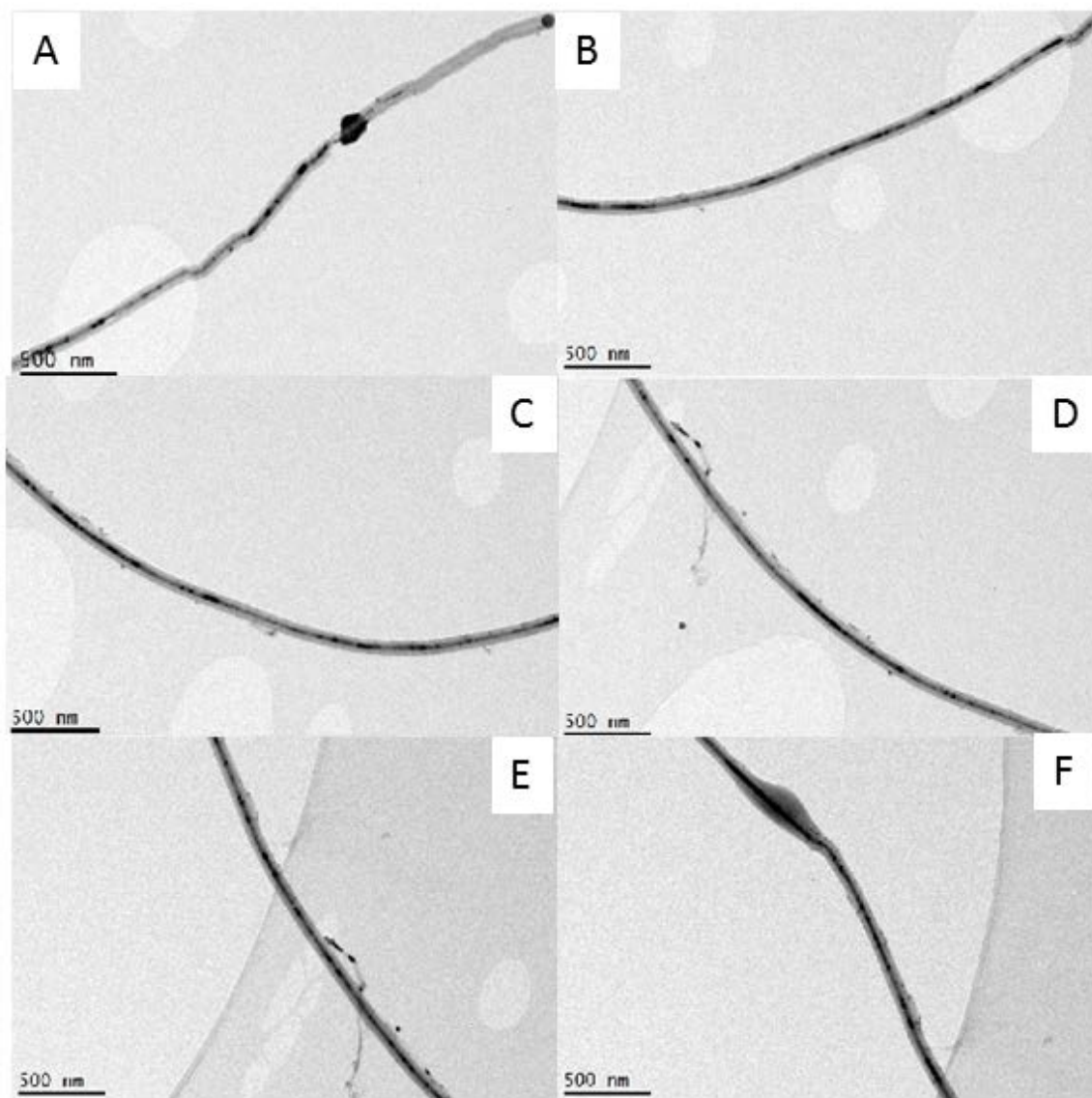
Fig.6: The A-F sequence of transmission electron micrographs follows a single radial filled multiwall-carbon-nanotube; the filling is continuous for ~9μm. The swelling feature in micrograph F is due to electron beam damage that resulted from the long exposure time needed to complete the sequence.
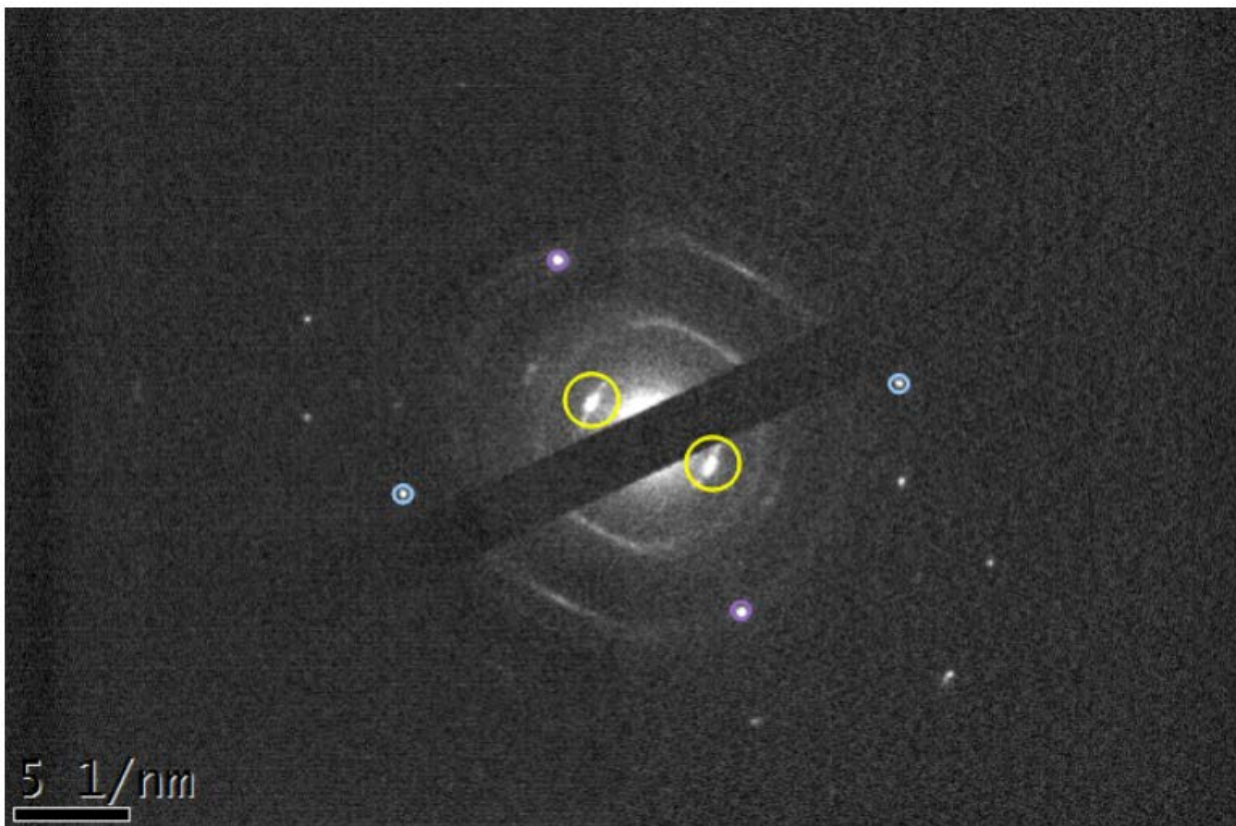
Fig.7: A typical selective area diffraction pattern obtained from a multiwall-carbon-nanotube encapsulated nanocrystal. The pale blue circles correspond to the (310) lattice planes (lattice spacing 0.09 nm) of α-Fe cubic (Im-3m, Crystal Open Database Ref. 1100108), while the violet circles correspond to the (211) lattice planes (lattice spacing 0.12 nm) of α-Fe cubic (*Im-3m*, Crystal Open Database Ref. 1100108). The yellow circles correspond to the (002) lattice planes of graphite (*P*63/*mmc*), lattice spacing 0.34 nm (ICSD Chemical Database Ref. 53781).
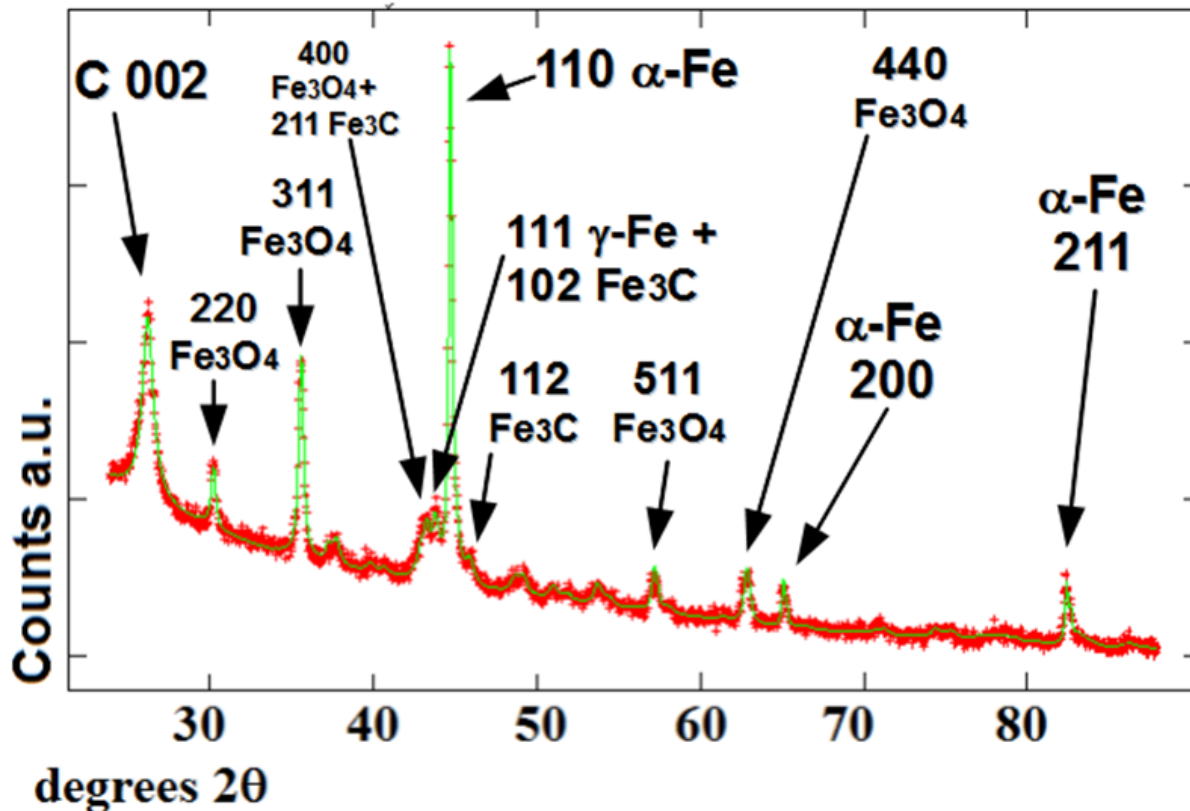
Fig.8: Typical X-ray diffractogram data (red), and Rietveld refinement (green line) for urchin powder obtained with an vapor flow rate of 3.5 ccm. Arrows denote the crystal planes attributed to each intensity peak. The relative weight abundance of the encapsulated phases are 3% cubic γ-Fe (Fm-3m, Crystal Open Database Ref. 9008469), and 12% of cubic α-Fe (Im-3m, Crystal Open Database Ref. 1100108) and 18 % of orthorhombic Fe_3C (Crystal Open Database Ref. Pnma 16593). A 17% weight abundance of Fe_3O_4 (cubic, space group FD3-MZ) results from spontaneous oxidation of non-encapsulated iron particles when the powder is handled in air.
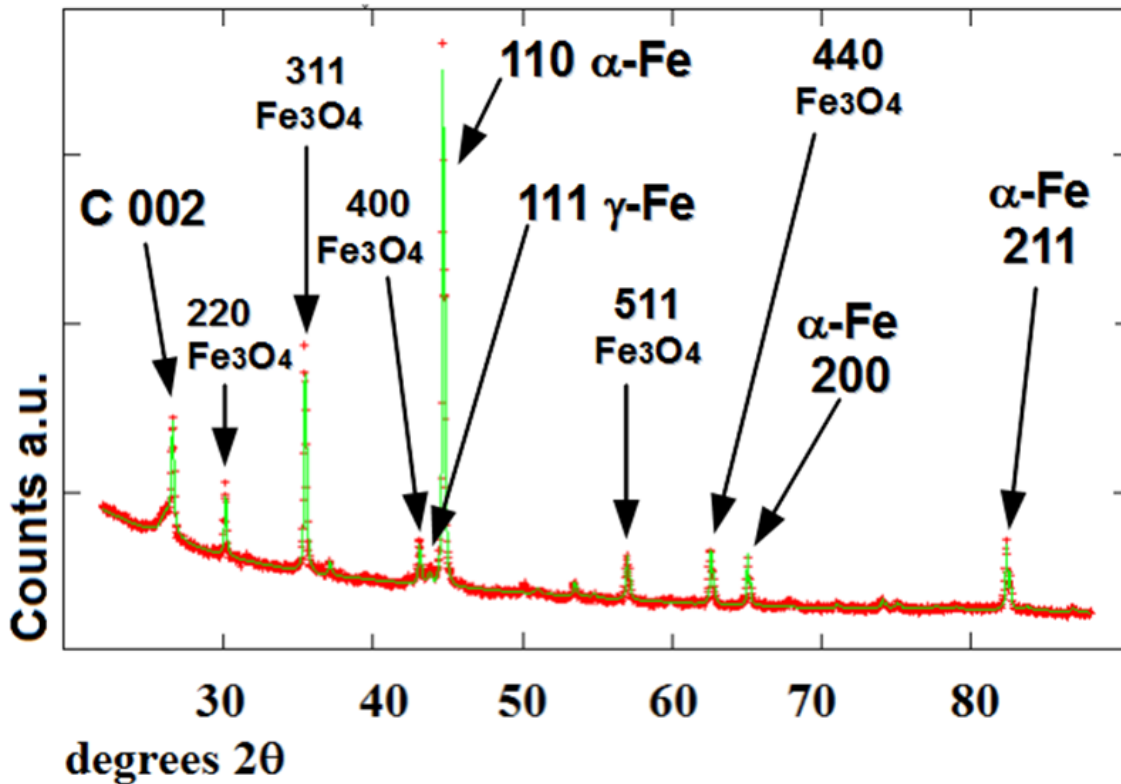
Fig.9: Typical X-ray diffractogram data (red), and Rietveld refinement (green line) for powder comprising urchins obtained with a vapor flow-rate of 20 ccm. Arrows denote the crystal planes attributed to each intensity peak. The relative weight abundance of the phases are 2% cubic γ-Fe (Fm-3m, Crystal Open Database Ref. 9008469), and 28% of cubic α-Fe (Im-3m, Crystal Open Database Ref. 1100108). A 26% weight abundance of Fe_3O_4 (cubic, space group FD3-MZ) results from spontaneous oxidation of non-encapsulated iron particles when the powder is handled in air.
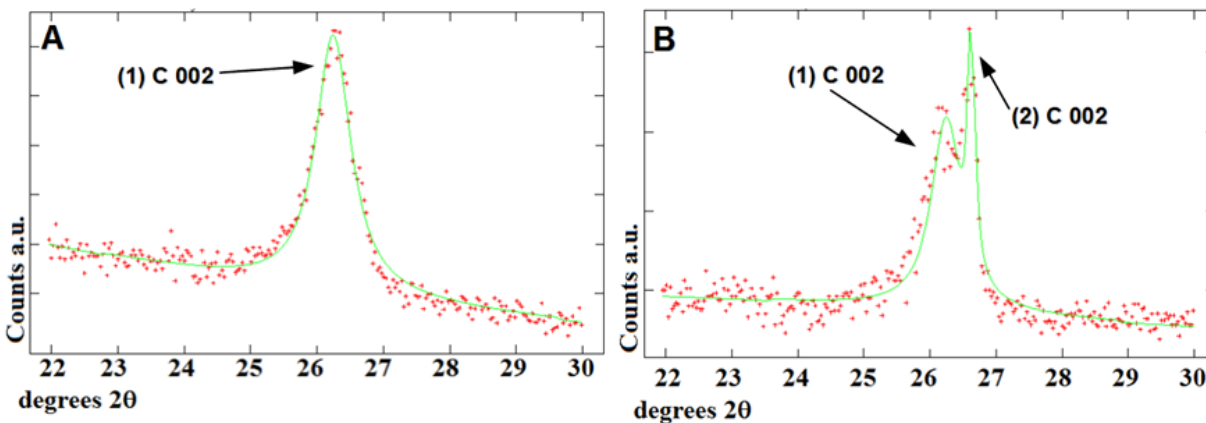
Fig.10: Typical X-ray diffractogram data (red), and Rietveld refinement (green line), of the 002 graphitic carbon reflection obtained from a powder comprising filled nanotube material grown on a smooth quartz surface (A) and from urchin powder prepared under identical reaction conditions (B). Clearly (B) shows two proximate peaks; the lower angle peak (1) corresponds to the 002 reflection from multiwall carbon nanotube walls observed in (A). This feature corresponds to the 0.34 nm lattice spacing directly observed in selective area diffraction studies of individual filled nanotube (Fig. 7), namely the 002 reflection from graphite space group P63/mmc (ICSD Chemical Database Ref. 53781). The second graphitic peak (2) corresponds to the lattice spacing of 0.33 nm (002 peak of graphite hexagonal *P*63/*mmc*, ICSD Chemical Database 52230) of the graphitic shell of the spherical particles as observed in the selective area diffraction pattern in Fig.5 (inset).

The field dependence of dc magnetization of as-produced urchin powder exhibited ferromagnetic hysteresis; at 5 K the saturation magnetization, M_s, showed a dependence on the vapor flow rate, with M_s(3.5 ccm) = 31 emu/g and M_s(20 ccm) = 13 emu/g, whereas the coercivity is almost constant: H_c(3.5 ccm)= 790 Oe, and H_c(20 ccm)= 843 Oe, Fig.11.

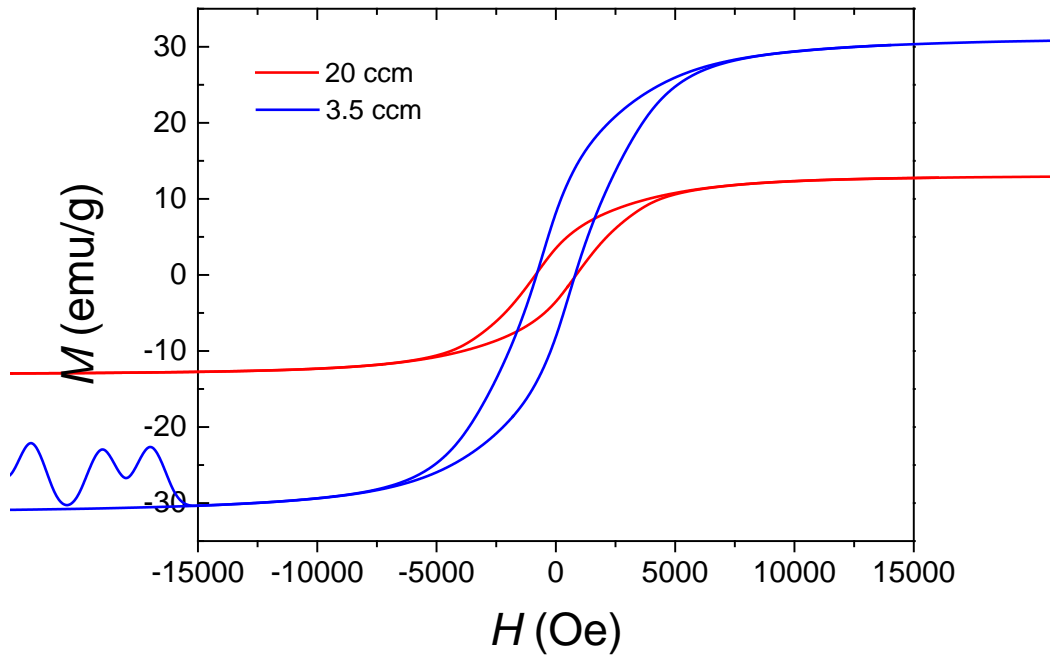Fig.11: The field dependence of dc magnetization at T=5 K of as-produced urchin powder for two values of the laminar vapor flow rate. The relative weight abundance for the powder produced with a flow rate of 3.5 ccm was 3% γ-Fe, 12% α-Fe, 18% Fe_3C, 17% Fe_3O_4, and 50% C (see Fig.8). The relative weight abundance for the powder produced with a flow rate of 20 ccm was 2% γ-Fe, 28% α-Fe, 26% Fe_3O_4, and 44% C (see Fig.9).

The relative weight abundance of the components found in the as-produced powder was extracted from the Reitveld analysis of the X-ray diffractograms, Fig. 8, 9. The γ-Fe contribution to the saturation magnetisation was then estimated by subtracting the weighted average of the saturation magnetization of bulk α-Fe ($M_s\sim$220 emu/g; Curie temperature, T_c= 1043 K), Fe_3C ($M_s\sim$169 emu/g, T_c= 483 K) [60, 61], Fe_3O_4 (M_s=92-100 emu/g, T_c= 850 K) [62], and the diamagnetic behavior of graphitic carbon (M=−0.7 emu/g at 50 kOe) [41]. This quantity was found to be always negative thus indicating an exchange-coupled ferromagnetic system despite only a small fraction of γ-Fe (the antiferromagnetic component): this conclusion agrees with that of Karmakar *et al.* for randomly oriented mainly α-Fe-filled carbon nanotubes with similarly low γ-Fe content (1%) [35]. The measured value of M_s (300 K)=28 emu/g was also comparable with that reported for randomly oriented vertical structures by Karmaker *et al*. (34 emu/g) [35]. The origin of the exchange coupling in γ-Fe/α-Fe-filled carbon nanotube systems has been the subject of much debate; interpretation of the data is difficult owing to the sample morphology and differing spatial distributions of the phases [27, 35, 63]. Moreover, theory predicts that γ-Fe can be antiferromagnetic, ferromagnetic, or nonmagnetic depending on lattice parameters or cluster-size [64].

We propose an urchin formation mechanism that accounts for the similarities to and differences from the vertical structures, Fig. 12. The similarity of encapsulated phases is a strong indication that local- and global-pathway carbon-to-metal ratios are similar. The latter is not surprising since, as stated previously, it is ultimately fixed by the composition of the decomposed molecule. The differences are remarkable: urchin morphology; homogeneous nucleation on an unusual central agglomeration, greater nanocrystal continuity; the carbon content varies with vapor flow

rate; the vapor flow rate is low relative to those used for vertical structure growth; urchin diameter uniformity; and self-sustaining formation conditions. The first conclusion that can be drawn is that thermodynamic fluctuations in the boundary layer are what produce the homogenous nucleation of the spherical graphite-encapsulated Fe_3C nanocrystals of the central agglomeration. All other aspects of urchin formation follow from this conclusion, Fig. 12. The defining features of the proposed mechanism are that all the diffusion gradients are spherically symmetric and the filled-carbon-nanotube growth is via a vapor feedstock supply to the open tips which is unimpeded by a near neighbor (in contrast with close-packed vertical structure formation) – this model is analogous to the instability points at the sharp features of a central ice crystal from which radial growth occurs due to unimpeded energy dissipation during snowflake formation. This tip growth must involve a temperature gradient exactly at the tip due to the endothermic nanotube formation since, unlike the vertical structures, not all of the urchin nanotubes grow in the natural temperature gradient of the reactor. This temperature gradient will also drive the carbon flow along the axis of the encapsulated nanocrystal toward the tip. These features account for the morphology, high degree of nanocrystal filling, and low vapor flow rate requirement (high flow rates will produce diffusion gradient asymmetries). The self-replication reaction conditions arise from the comparable conditions at the laminar-viscous boundary as fully formed urchins accumulate on the surface. This model suggests that the migration time increases with increasing vapor flow rate, since vapor velocities are higher at the laminar-viscous boundary, so the carbon content of the encapsulated nanocrystals will decrease with flow rate owing to the longer lifetime of the temperature gradient at the nanotube tips; this is in agreement with the observations described above.
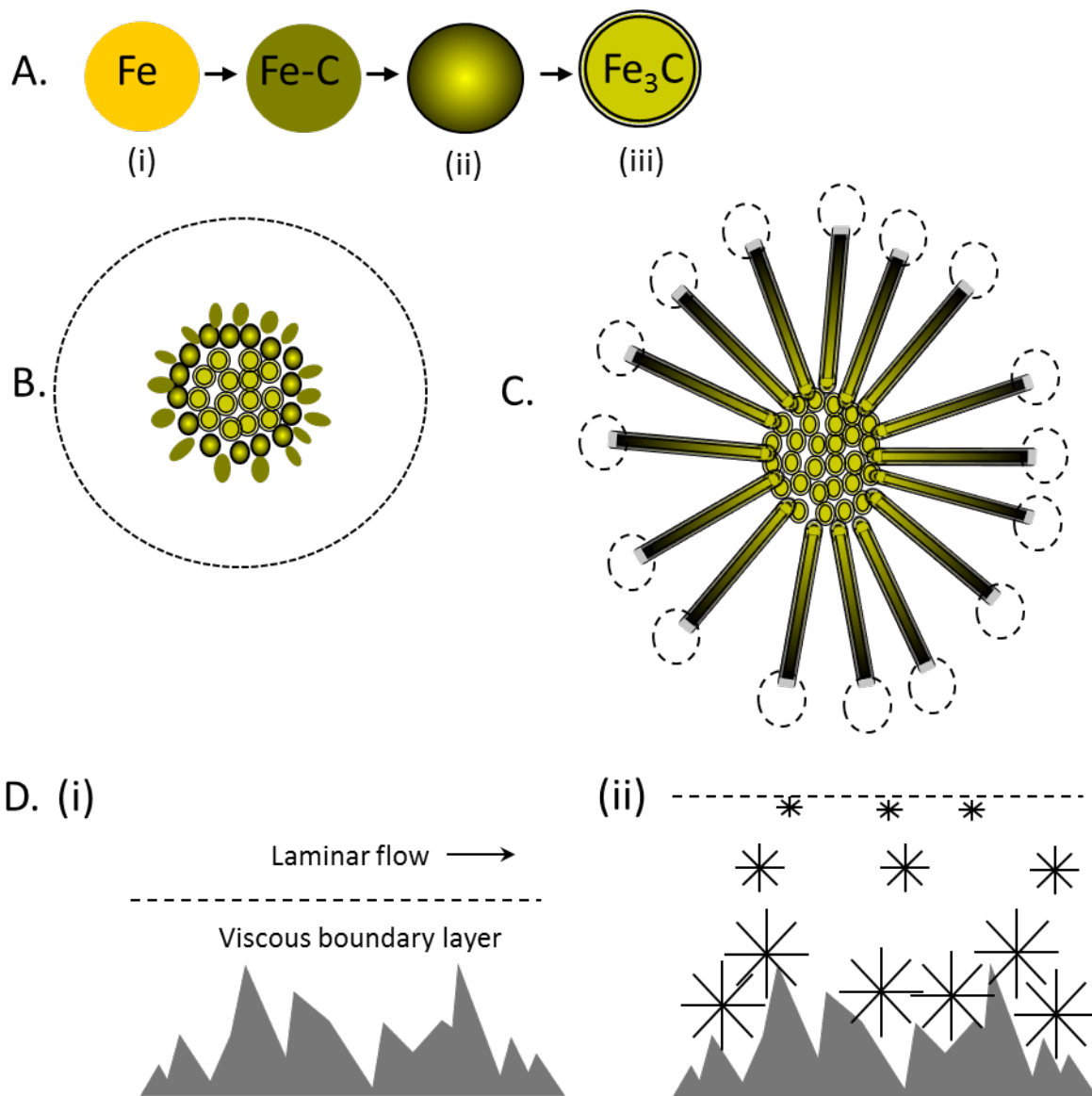
Fig. 12. A schematic diagram of the proposed three-stage urchin formation mechanism in fluctuating metal-carbon vapor. Yellow shading implies high iron content; solid black lines and dark shading represent graphitic carbon and the carbon-richness of a nanoparticle respectively. The dashed lines represent the volume of vapor within several diffusion lengths (for the metal-carbon species in the vapor) from the active area of formation. A: (i) The graphite-encapsulated Fe_3C particles spontaneously form by homogeneous nucleation of Fe or Fe-C particles in the

vapor, (ii) carbon feedstock is driven to particle by the resultant diffusion gradient and dissolves in the particle, (iii) graphitic carbon shells form when the rate of arrival of the carbon feedstock exceeds the rate of dissolution, (iv) flow of internal carbon is driven to the surface by the endothermic formation of the graphitic shells but is ceases when the stable Fe_3C nanocrystal composition is reached. B: These spherical structures spontaneously agglomerate; the central particles are encapsulated (stage A (iii)) whereas the peripheral particles have no graphitic shell (stage A (i)). The spherical diffusion gradient created by the agglomeration results in an asymmetry in the vapor feedstock for the peripheral particles which results in elongation. C: The lowest energy stable graphitic carbon structure for the elongated peripheral particles is a carbon nanotube. The central-particle-facing face of the elongated peripheral particles is rapidly closed by graphitic shell formation consequently the radial growth of the filled nanotubes is driven by the diffusion gradient established at the open tip. This diffusion gradient must be partially driven by a temperature gradient because, unlike the vertical structures, not all of the radial nanotubes are growing in the natural temperature gradient of the reactor. D: Self-sustaining reaction conditions can be explained as follows. (i) A rough surface produces randomly fluctuating vapor in the boundary layer between the rough surface and the global laminar flow. (ii) The diameter uniformity of the central particle and urchin suggests that nucleation occurs at the laminar-viscous interface since this is the realm of weak fluctuations and uniform feedstock supply from the global flow; after nucleation, the spherically symmetric diffusion gradients define the local feedstock supply to the nanotubes which serve to damp the local fluctuations in the boundary layer, subsequent urchin formation in the boundary layer is therefore uniform. Attractive forces on the urchin due to the proximity of the rough surface are greater than the thermophoretic forces so the structure migrates to the rough surface. The period of migration therefore dictates the

diameter of the urchin. Once in contact with the surface the formation process will cease because the isothermal surface will equilibrate the temperature gradients at the tips. The roughness of the urchin coating of the surface replicates that of the pristine rough surface, consequently the conditions for nucleation and the laminar-viscous boundary are reproduced.

This method of synthesis therefore exploits thermodynamic fluctuation in a local pathway. One of the principal advances in the understanding of non-equilibrium thermodynamic systems is that the onset of self-organization is dictated by the behavior of fluctuations: order is propagated by amplification of these fluctuations through a feedback mechanism involving interaction with the global environment [65]. We have shown that the nucleation and subsequent growth of the radial structure results from fluctuation-amplification by exchange of vapor feedstock and thermal energy with the environment. From the thermodynamic point of view, the success of the method results from the magnitude of the thermodynamic fluctuation. If near-to-equilibrium conditions are established then the dynamics and rates of chemical reaction remain linear and the reaction products resemble those produced in equilibrium conditions [65]. However, far-from-equilibrium conditions are characterized by non-linearity in most aspects of reaction-diffusion system behavior; therefore, the reaction product will be unpredictable [66]. The logic of these arguments is that the laminar-viscous interface could be the source of ordered and unusual nanoscale reaction products.

The outstanding feature of boundary layer chemical vapor synthesis that distinguishes it from arc, CVD, or aerosol methods is that random fluctuation in local pathways results in a single self-organized, spherically symmetric product dominating the reactor. This is a simple, scalable method which does not require ultra-fine control of process parameters or any highly-engineered reactor components. Since the most significant global variable, the carbon-to-metal ratio, can be changed by selection of the molecular species or using multiple carbon-metal sources (as done in the conventional CVD) we can be optimistic that the method can be used to synthesize the other unusual nanoscale structures from the unified product map. None of the processes that underpin

the self-organization is unique to carbon-metal systems therefore there is no fundamental reason why the method cannot be used to produce nanoscale structures that self-organize by a vapor-, liquid-, solid-phase process from other vapor systems. The task for the experimenter is to identify the optimal conditions at the laminar-viscous boundary for the desired product formation.

These ferromagnetically filled-carbon-nanotube urchins have potential for applications which exploit the high surface area and the high volume fraction of ferromagnetic material of an individual urchin, for example as magnetic nanocomposite fillers, microwave absorbing materials, and magnetic particles for magnetorheological fluids. The structures could have promise for magnetic hyperthermia applications since the urchin morphology guarantees ferromagnetic nanowire alignment with an external magnetic field in any direction [67].

4. Conclusion

Radial growth of self-organized filled-carbon-nanotubes was achieved for the first time by new chemical vapor synthesis method based on self-organization at the interface between a viscous boundary layer and a laminar vapor flow. The method is simple, scalable and does not require ultra-fine control of process parameters or any highly-engineered reactor components. The radial structures comprise multiwall carbon nanotubes, encapsulating >9 μm-long nanocrystals of α-Fe and γ-Fe phases, departing from a central particle comprising an agglomeration of spherical graphite-encapsulated Fe_3C nanocrystals. We propose a formation mechanism which is based on experimental observations for both the radial structures and the equivalent vertical structures that

form on smooth surfaces under identical conditions. We argue that the laminar-viscous vapour flow boundary is very conducive to the self-organized formation of metal-carbon nanostructures.

References

[1] Dresselhaus MS, Dresselhaus G, Eklund PC. Science of Fullerenes and Carbon Nanotubes, Academic Press 1996

[2] Elliott BR, Host JJ, Dravida VP, Teng MH, Hwang J-H. A Descriptive Model Linking Possible Formation Mechanisms for Graphite-Encapsulated Nanocrystals to Processing Parameters. J. Mater. Res. 1997; 12(12): 3328-44

[3] Jones AC, Hitchman ML (Eds.) Chemical Vapour Deposition: Precursors, Processes, and Applications. RSC Publishing 2008

[4] Wagner RS, Ellis WC. Vapour-Liquid-Solid Mechanism of Single Crystal Growth. Appl. Phys. Lett. 1964; 4(5): 89-90

[5] Harutyunyan AR, Kuznetsov OA, Brooks CJ, Mora E, Chen G. Thermodynamics Behind Carbon Nanotube Growth *via* Endothermic Catalytic Decomposition Reaction. ACS Nano 2009; 3(2): 379-85

[6] Moisala A., Nasibulin AG, Kauppinen EI. The Role of Metal Nanoparticles in the Catalytic Production of Single-Wall Carbon Nanotubes – a Review. J. Phys. Condens. Matter. 2003; 15: S3011-35

[7] Kumar M, Ando Y. Chemical Vapor Deposition of Carbon Nanotubes: A Review on Growth Mechanism and Mass Production. J. Nanosci. Nanotechnol. 2010; 10(6): 3739-58

[8] Rodriguez NM. A Review of Catalytically Grown Carbon Nanofibers. J. Mater. Res. 1993; 8(12): 3233-50

[9] Thostenson ET, Li WZ, Wang DZ, Ren ZF, Chou TW. Carbon Nanotube/Carbon Fiber Hybrid Multiscale Composites. Appl. Phys. 2002; 91(9): 6034-37

[10] Subramoney S, Ruoff RS, Lorents DC, Malhotra R. Radial Single-Layer Nanotubes. Nature 1993; 366: 637

[11] Sato Y, Monomiya K, Jayadevan B, Tohji K, Sato G, Ishida H, et al. Effect of Cerium Ions in An Arc Peripheral Plasma on the Growth of Radial Single-Walled Carbon Nanotubes. J. Appl. Phys. 2005; 98(9): 094313

[12] Kumar Y, Ando Y. Controlling the Diameter Distribution of Carbon Nanotubes Grown from Camphor on a Zeolite Support. Carbon 2005; 43(3): 533-40

[13] Piao YZ, An KJ, Kim JY, Yu TY, Hyeon TH. Sea Urchin Shaped Carbon Nanostructured Materials: Carbon Nanotubes Immobilized on Hollow Carbon Spheres. J. Mater. Chem. 2006; 16(29): 2984-89

[14] Zhang Q, Huang J-Q, Zhao M-Q., Qian W-Z, Wang Y, Wei F. Radial Growth of Vertically Aligned Carbon Nanotube Arrays from Ethylene on Ceramic Spheres. Carbon 2008; 46(8): 1152-58

[15] Hwang EJ, Lee SK, Jeong MG, Lee YB, Lim DS. Synthesis of Sea Urchin-Like Carbon Nanotubes on Nano-Diamond Powder. J. Nanosci. and Nanotech. 2012; 12(7): 5875–79

[16] Nguyen XH, Lee YB, Lee CH, Lim DS. Synthesis of Sea Urchin-like Particles of Carbon Nanotubes Directly Grown on Stainless Steel cores and Their Effect on the Mechanical Properties of Polymer Composites. Carbon 2010; 48(10): 2910-16

[17] Moon YK, Lee J, Lee JK, Kim TK, Kim SH. Synthesis of Length-Controlled Aerosol Carbon Nanotubes and Their Dispersion Stability in Aqueous Solution. Langmuir 2009; 25(3): 1739-43

[18] Weissker U, Hampel S, Leonhardt A, Buchner B. Carbon Nanotubes Filled with Ferromagnetic Materials. Materials 2010; 3: 4387- 427

[19] Sen R, Govindaraj A, Rao CNR. Carbon Nanotubes by the Metallocene Route. Chem. Phys. Lett. 1997; 267(3-4): 276-80

[20] Rao CNR., Sen R, Satishkumar BC, Govindaraj A. Large Aligned-Nanotube Bundles from Ferrocene Pyrolysis. Chem. Comm. 1998; 15: 1525-26

[21] Grobert N, Mayne M, Terrones M, Sloan J, Dunin-Borkowski RE, Kamalakaran R, et al. Alloy Nanowires: Invar Inside Carbon Nanotubes. Chem. Commun. 2001; 5:471-72

[22] Cao A, Zhang X, Wei J, Li Y, Xu C, Liang J, et al. Macroscopic Three-Dimensional Arrays of Fe Nanoparticles Supported in Aligned Carbon Nanotubes. J. Phys. Chem. B 2001; 105(48): 11937-40

[23] Elías AL, Rodríguez JA, McCartney MR, Golberg D, Zamudio A, Baltazar SE, et al. Production and Characterization of Single-Crystal FeCo Nanowires Inside Carbon Nanotubes. Nano Lett. 2005; 5(3): 467- 72

[24] Wang W, Wang K, Lv R, Wei J, Zhang X, Kang F. et al. Synthesis of Fe-Filled Thin-Walled Carbon Nanotubes with High Filling Ratio by Using Dichlorobenzene as Precursor. Carbon 2007, 45(5): 1105-36

[25] Kuwana K, Saito K. Modelling CVD Synthesis of Carbon Nanotubes: Nanoparticle Formation from Ferrocene. Carbon 2005; 43(10): 2088–95

[26] Marco JF, Gancedo JR, Hernando A, Crespo P, Prados C, Gonzalez JM. et al. Mossbauer Study of Iron-Containing Carbon Nanotubes. Hyperfine Interactions 2002; 139: 535-42

[27] Prados C, Crespo P, Gonzalez JM, Hernando A, Marco JF, Gancedo R, et al. Hysteresis Shift in Fe-filled Carbon Nanotubes due to γ-Fe. Physical Review B 2002; 65: 113405

[28] Goldberg D, Mitome M, Muller Ch, Tang C, Leonhardt A, Bando Y. Atomic Structures of Iron-based Single-crystalline Nanowires Crystallized Inside Multi-walled Carbon Nanotubes as Revealed by Analytical Electron Microscopy. Acta Materialia 2006; 54: 2567-76

[29] Muller C, Golberg D, Leonhardt A, Hampel S, Buchner B. Growth studies, TEM and XRD Investigations of Iron-filled Carbon Nanotubes. Physica status solidi (a) 2006; 203: 1064-8

[30] Weissker U, Loffler M, Wolny F, Lutz MU, Scheerbaum N, Klingeler R, et al. Perpendicular Magnetization of Long Iron Carbide Nanowires Inside Carbon Nanotubes due to Magnetocrystalline Anisotropy. Journal of Applied Physics 2009; 106: 054909

[31] Lutz MU, Weissker U, Wolny F, Muller C, Loffler M, Muhl T, et al. Magnetic Properties of α-Fe and Fe_3C Nanowires. Journal of Physics: Conference Series 2010; 200: 072062

[32] Ruskov T, Spirov I, Ritschel M, Muller C, Leonhardt A, Ruskov R. Mossbauer Morphological Analysis of Fe-filled Multiwalled Carbon Nanotube Samples. Journal of Applied Physics 2006; 100: 084326

[33] Leonhardt A, Ritschel M, Elefant D, Mattern N, Biedermann K, Hampel S, et al. Enhanced Magnetism in Fe-filled Carbon Nanotubes Produced by Pyrolysis of Ferrocene. Journal of Applied Physics 2005; 98: 074315

[34] Gui X, Wei J, Wang K, Wang W, Lv R, Chang J, et al. Improved Filling Rate and Enhanced Magnetic Properties of Fe-filled Carbon Nanotubes by Annealing and Magnetic Separation. Materials Research Bulletin 2008; 43: 3441-6

[35] Karmakar S, Sharma S M, Mukadam M D, Yusuf S M, Sood A K. Magnetic Behaviour of Iron-filled Multiwalled Carbon Nanotubes. Journal of Applied Physics 2005; 97: 054306

[36] Shi C X, Cong H T. Tuning the Coercivity of Fe-filled Carbon-nanotube Arrays by Changing the Shape Anisotropy of the Encapsulated Fe Nanoparticles. Journal of Applied Physics 2008; 104: 034307

[37] Morelos-Gomez A, Lopez-Urıas F, Munoz-Sandoval E, Dennis C L, Shull R D, Terrones H, et al. Controlling High Coercivities of Ferromagnetic Nanowires Encapsulated in Carbon Nanotubes. Journal of Materials Chemistry 2010; 20: 5906-14

[38] Dillon F C, Bajpai A, Koos A, Downes S, Aslam Z, Grobert N. Tuning the Magnetic Properties of Iron-filled Carbon Nanotubes. Carbon 2012; 50: 3674-81

[39] Groudeva-Zotova S., Kozhuharova R., Elefant D., Mühl T., Schneider C.M., Mönch I. Phase Composition and Magnetic Characteristics of Fe-Filled Multi-Walled Carbon Nanotubes. Journal of Magnetism and Magnetic Materials 2006; 306(1): 40–50

[40] Shpak AP, Kolesnik SP, Mogilny GS, Petrov Y N, Sokhatsky VP, Trophimova LN, et al. Structure and Magnetic Properties of Iron Nanowires Encased in Multiwalled Carbon Nanotubes. Acta Materialia 2007; 55(5): 1769–78

[41] Likodimos V, Glenis S, Guskos N, Lin CL. Magnetic and Electronic Properties of Multiwall Carbon Nanotubes. Phys. Rev. B 2003; 68(4): 045417

[42] Shi CX, Cong HT. Tuning the Coercivity of Fe-Filled Carbon-Nanotube Arrays by Changing the Shape Anisotropy of the Encapsulated Fe Nanoparticles. J. Appl. Phys. 2008; 104(3): 034307

[43] Morelos-Gómez A, López-Urías F, Muňoz-Sandoval E, Dennis CL, Shull RD, Terrones H, et al. Controlling High Coercivities of Ferromagnetic Nanowires Encapsulated in Carbon Nanotubes. J. Mater. Chem. 2010; 20(28): 5906-14

[44] Dillon FC, Bajpai A, Koós A. Downes S, Aslam Z, Grobert N. Tuning the Magnetic Properties of Iron-Filled Carbon Nanotubes. Carbon 2012; 50(10): 3674-81

[45] Terrones H, López-Urías F, Munoz-Sandoval E, Rodríguez-Manzo JA, Zamudio A, Elías AL, et al. Magnetism in Fe-Based and Carbon Nanostructures: Theory and Applications. Solid State Sciences 2006; 8(3-4): 303–20

[46] Klingeler R, Sim RB. (Eds.) Carbon Nanotubes for Biomedical Applications. Springer 2011

[47] Watts PCP., Hsu WK, Randall DP, Kotzeva V, Chen GZ. Fe-Filled Carbon Nanotubes: Nano-Electromagnetic Inductors. Chem. Mater. 2002; 14(11): 4505–08

[48] Wolny F, Mühl T, Weissker ., Lipert K, Schumann J, Leonhardt A. et al. Iron Filled Carbon Nanotubes as Novel Monopole-Like Sensors For Quantitative Magnetic Force Microscopy. Nanotechnology 2010; 21(43): 435501-06

[49] Hudziak S, Darfeuille A, Zhang R, Peijs T, Mountjoy G, Bertoni G. et al. Magnetoresistive Phenomena in Fe-Filled Carbon Nanotube/Elastomer Composites. Nanotechnology 2010; 21(12): 125505

[50] Lv R, Tsuge S, Gui X, Takai K, Kang F, Enoki T. et al. In Situ Synthesis and Magnetic Anisotropy of Ferromagnetic Buckypaper. Carbon 2009; 47(4): 1141-5

[51] Lin H, Zhu H, Guo H, Yu L. Investigation of the Microwave-Absorbing Properties of Fe-Filled Carbon Nanotubes. Materials Letters 2007; 61(16): 3547–50

[52] Che R, Peng LM, Duan X, Chen Q, Liang X. Microwave Absorption Enhancement and Complex Permittivity and Permeability of Fe Encapsulated Within Carbon Nanotubes. Adv. Mater. 2004; 16(5): 401-05.

[53] Sano N, Naito M, Kikuchi T. Enhanced Field Emission Properties of Films Consisting of Fe-core Carbon Nanotubes Prepared Under Magnetic Field. Carbon 2007; 45(1): 78-82.

[54] Weißker U, Muhl T, Leonhardt A. , Buchner B. Room Temperature Magnetometry of an Individual Iron Filled Carbon Nanotube Acting as Nanocantilever. J. Appl. Phys. 2011; 110(8): 084319.

[55] Perry AE, Schofield WH, Joubert PN. Rough Wall Turbulent Boundary Layers. J. Fluid Mech. 1969; 37(2): 383-412

[56] Holman JP. Heat Transfer. McGraw-Hill 2002

[57] Ruoff RS, Lorents DC, Chan B, Malhotra R, Subramoney S. Single Crystal Metals Encapsulated in Carbon Nanoparticles. Science 1993; 259(5093): 346-48

[58] Lu Y, Zhu Z, Liu Z. Carbon-Encapsulated Fe Nanoparticles from Detonation-Induced Pyrolysis of Ferrocene. Carbon 2005; 43(2): 369–74

[59] Ermakova MA, Ermakov DY, Chuvilin AL, Kuvshinov GG. Decomposition of Methane over Iron Catalysts at the Range of Moderate Temperatures: The Influence of Structure of the Catalytic Systems and the Reaction Conditions on the Yield of Carbon and Morphology of Carbon Filaments. J. Catalysis 2001; 201(2):183-197

[60] Tebble S, Craik DJ. Magnetic Materials. Wiley, New York 1966

[61] Häglund J, Grimvall G, Jarlborg T. Electronic Structure, X-ray Photoemission Spectra, and Transport Properties of Fe_3C (Cementite). Phys. Rev. B 1991; 44(7): 2914-19

[62] Goya GF, Berquo TS, Fonseca FC, Morales MP. Static and Dynamic Magnetic Properties of Spherical Magnetite Nanoparticles. J. Appl. Phys. 2003; 94(5): 3520–28

[63] Mühl T, Elefant D, Graff A, Kozhuharova R, Leonhardt A, Mönch I, Ritschel M, Simon P, Groudeva-Zotova S, Schneider CM. Magnetic Properties of Aligned Fe-filled Carbon Nanotubes. J. Appl. Phys.2003; 93(10): 7894-96

[64] Wang CS, Klein BS, Krakauer H. Theory of Magnetic Structural Ordering in Iron. Phys. Rev. Lett. 1985; 54(16): 1852-55

[65] Nicolis G, Prigogine I. Self-Organization in Nonequilibrium Systems: From Dissipative Structures to Order Through Fluctuations. Wiley 1977

[66] Grzybowski BA. Chemistry in Motion. Wiley, 2009

[67] Mamia H, Jeyadevan B. Hyperthermic Effects of Dissipative Structures of Magnetic Nanoparticles in Large Alternating Magnetic Fields. Sci. Rep. 2011; 1: 157